Analytical Methods

Accepted Manuscript

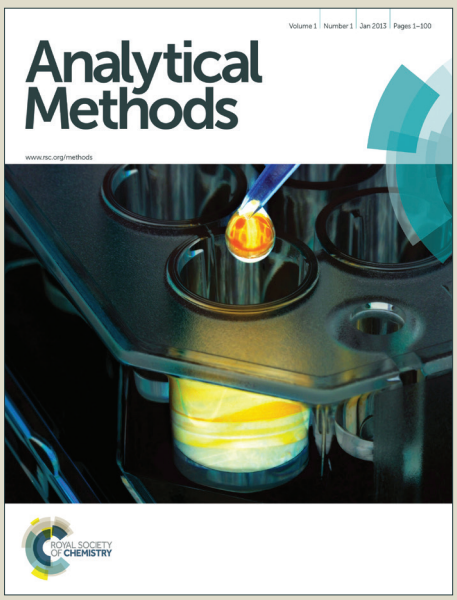

ROYAL SOCIETY OF CHEMISTRY

www.rsc.org/methods

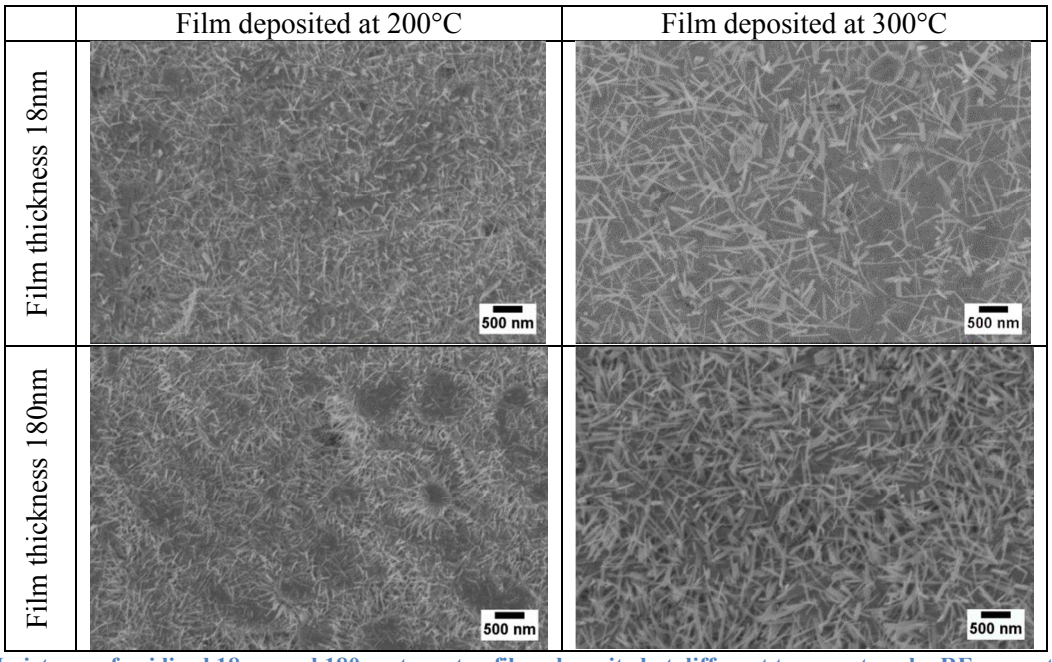

Table 1: SEM pictures of oxidized 18nm and 180nm tungsten films deposited at different temperature by RF magnetron sputtering.

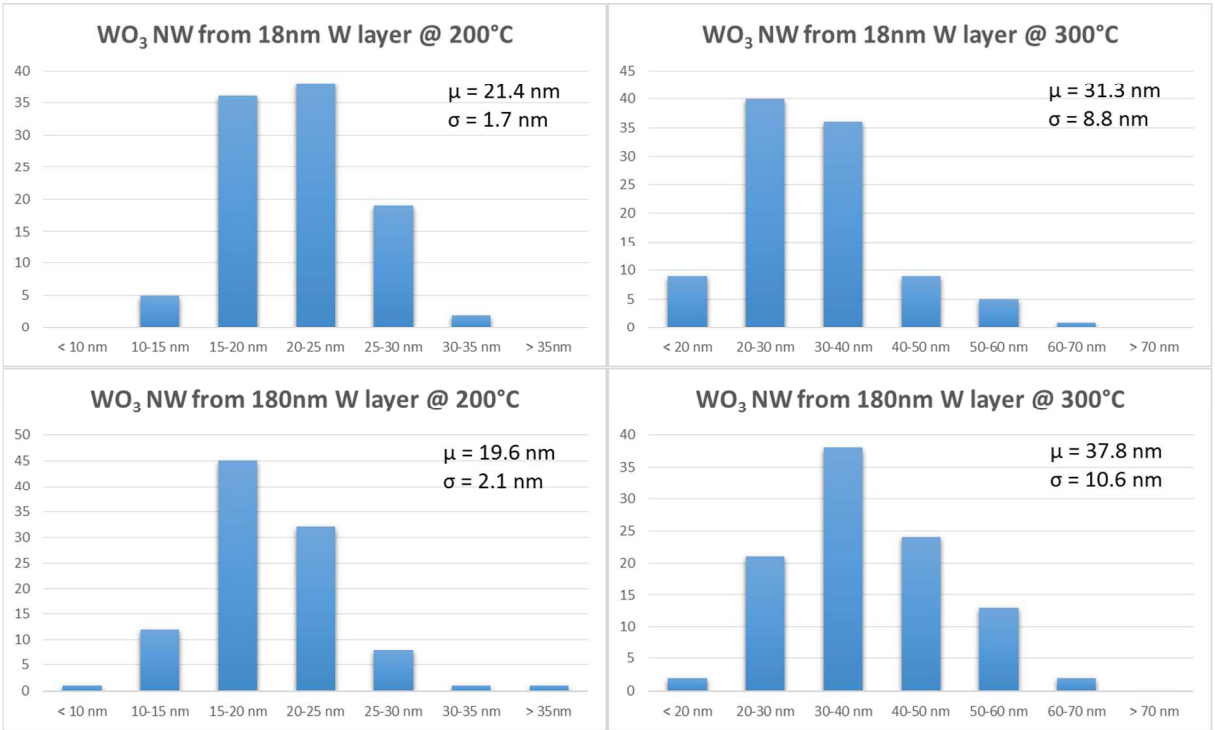

Figure 1: Diameter distribution of WO_3 NWs grown on alumina substrate starting from different metallic W layers.

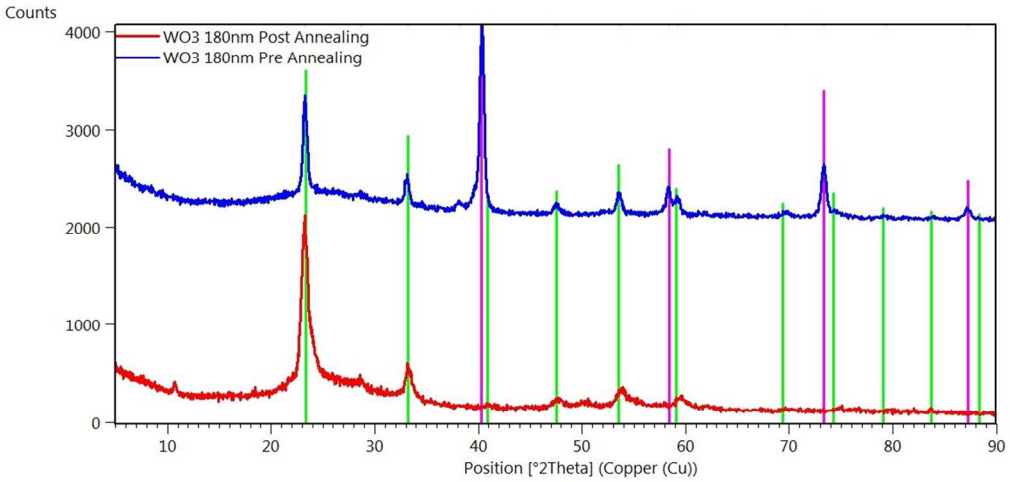

Figure 2: X-Ray Diffraction (XRD) spectra of WO_3 180nm before (blue) and after annealing (red), and reference peaks of metallic W (magenta) and WO_3 (green). Spectra shifted in intensity for clarity purpose.

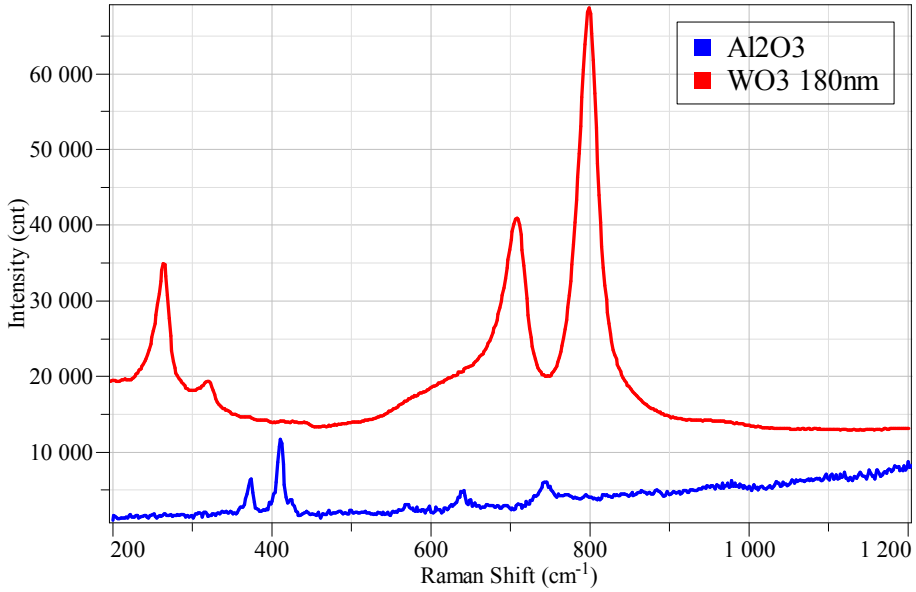

Figure 3: Raman spectra of WO_3 180nm and alumina substrate. Spectra shifted in intensity for clarity purpose.

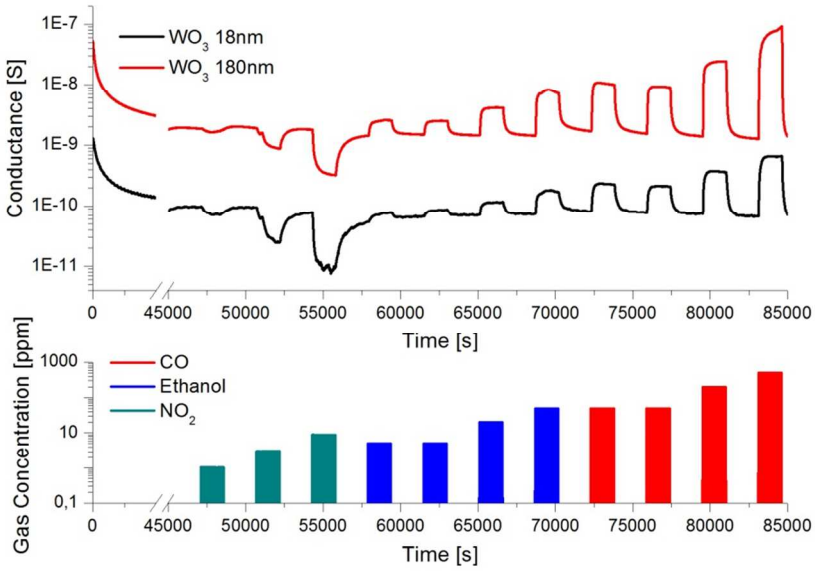

Figure 4: Dynamic response of WO_3 sensing devices towards some oxidizing and reducing gas chemical compound, measured at 200°C with a relative humidity of 50% @ 20°C.

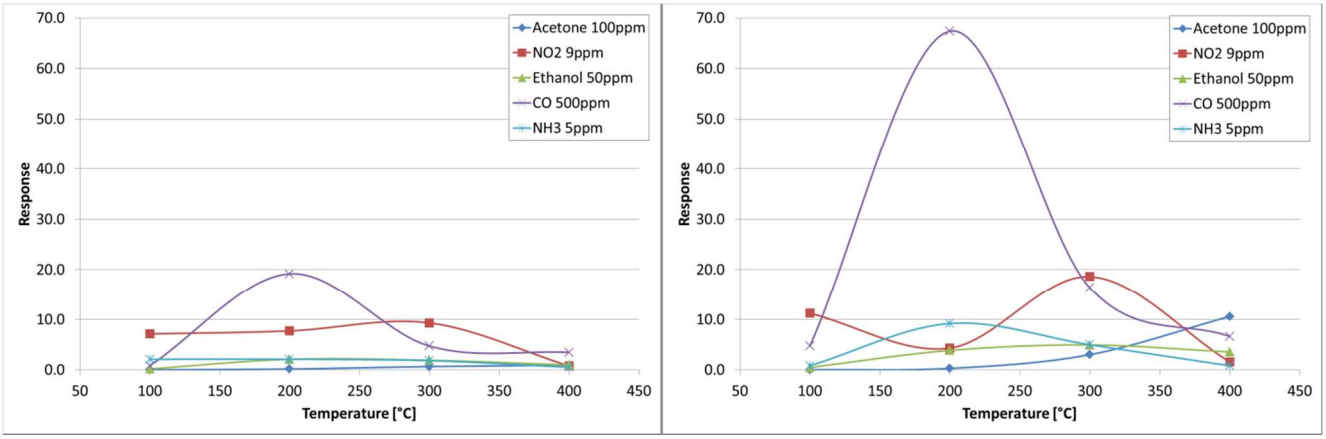

Figure 5: Temperature dependence of the response of 18nm (left) and 180nm (right) WO_3 nanostructures, measured with a relative humidity of 50% @ 20°C.

	Working Temperature	Detection Limit	B	A
CO	200 °C	13 ppm	1.15	0.05
NO2	100 °C	1 ppm	1.23	0.87
NH3	200 °C	1.5 ppm	2.04	0.5

Table 2: Power trend line coefficients and detection limits towards CO, NO_2 and NH_3.

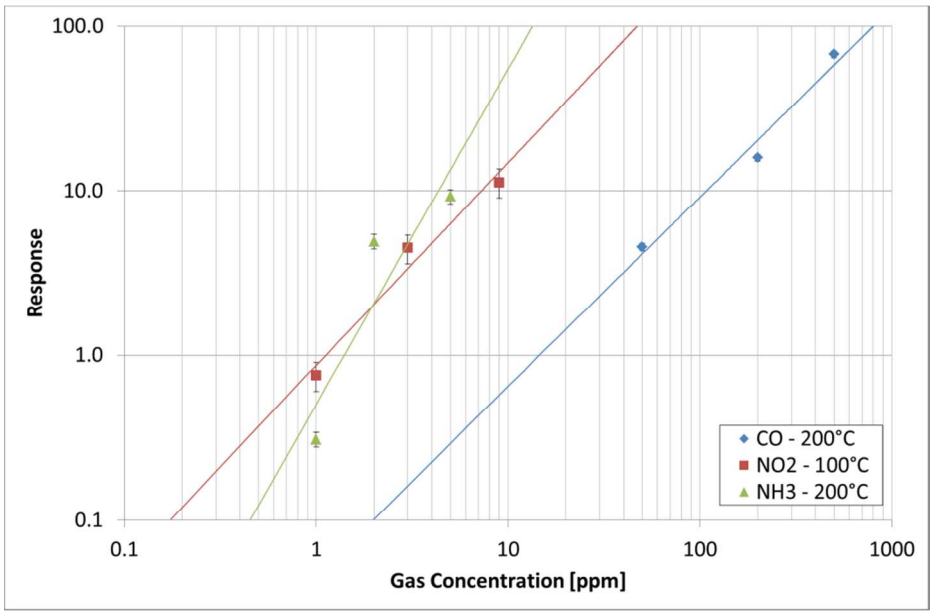

Figure 6: Detection trend lines for 180nm devices towards CO, NO_2 and NH_3. Relative humidity was 50% @ 20°C

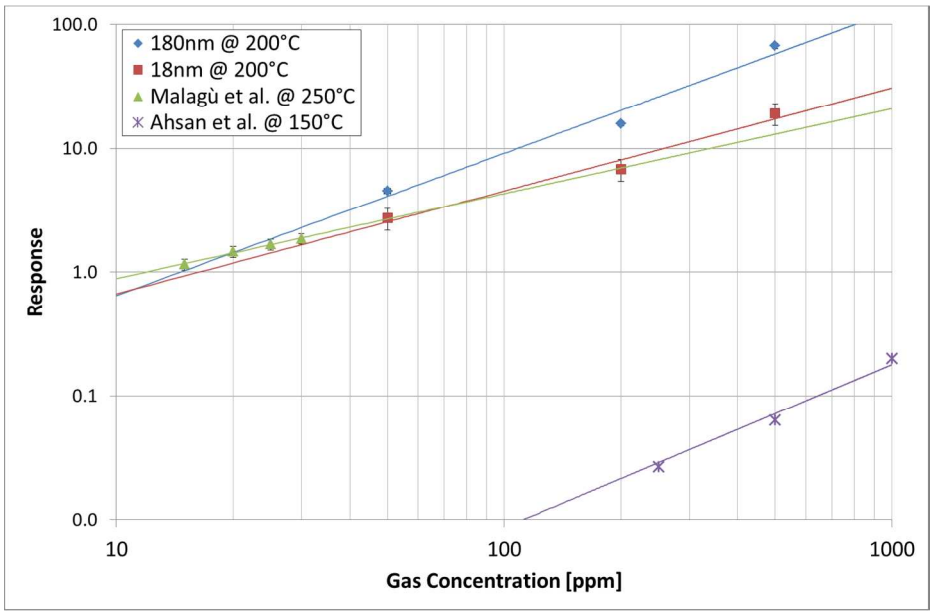

Figure 7: Carbon monoxide (CO) sensing performance comparison between fabricated WO_3 nanostructures (18 nm and 180 nm) and reference literature, in particular *Ahsan et al.* [3] and *Malagù et al.* [24].

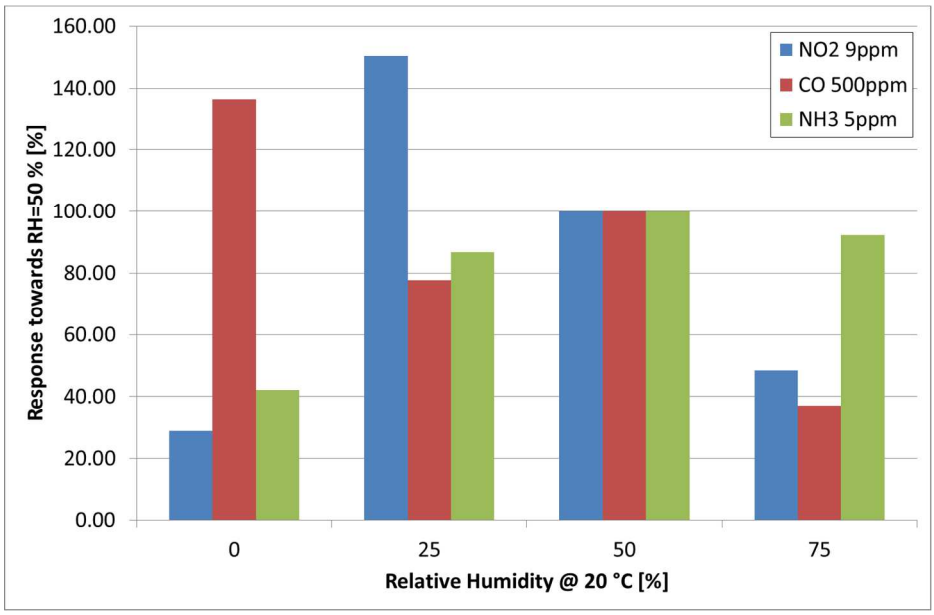

Figure 8: Influence of humidity on WO_3 180nm device response towards nitrogen dioxide, carbon monoxide and ammonia. On the y-axis the ratio between the response at the target value of relative humidity respect the reference value of RH=50% @ 20°C. Sensors temperature fixed @ 200°C.

Analytical Methods

RSCPublishing

ARTICLE

Tungsten oxide nanowires for chemical detection

Cite this: DOI: 10.1039/xoxxoooooox

D. Zappa, A. Bertuna, E. Comini, M. Molinari, N. Poli, G. Sberveglieri

SENSOR Laboratory, University of Brescia and CNR-INO, Via Valotti 9, 25133 Brescia, Italy

Received ooth January 2012,
Accepted ooth January 2012

DOI: 10.1039/xoxxoooooox

www.rsc.org/

Tungsten oxide nanowires have been synthetized on alumina substrates in order to fabricate sensing devices. Metallic tungsten films have been deposited by RF magnetron sputtering and then oxidized in a controlled atmosphere, in order to obtain a dense mat of nanowires. Two batches of samples have been prepared, starting from 18nm and 180nm tungsten film, and the influence of the sputtering temperature on the morphology has been investigated. Raman and XRD spectroscopy were used to confirm the crystalline structure of the material. Chemical sensing performance of n-type tungsten oxide nanowires have been evaluated towards some oxidizing and reducing species, together with the influence of relative humidity. Fabricated WO3 nanowires exhibit a very good sensitivity, especially for the detection of NH3, NO2 and CO.

A Introduction

Tungsten oxides are a family of materials that have many interesting physical and chemical properties, which makes them ideal candidates for a number of different applications, ranging from field emitters [1, 2] to electrochromic[3] and chemical sensing devices [4-8]. Among the different oxides, tungsten trioxide WO_3 is probably the most studied one.

Tungsten trioxide is an n-type semiconductor that exhibits a wide bandgap of 2.7 eV [7]. This oxide is rather complex, and can crystallize in a number of different phases and crystal structures [9, 10], according to the temperature. The most stable one at room temperature has monoclinic structure, but at high temperature it can transform to orthorhombic [9]. Under certain conditions, it is possible to obtain tetragonal and hexagonal phases [11].

In literature, many different approaches are reported for the preparation of WO_3 thin films. Rather few studies focus on the synthesis of quasi 1D nanostructures, instead. The most common techniques for the synthesis of films and nanostructures are hydrothermal and solvothermal methods [12], thermal oxidation [1, 2], Pulsed Laser Deposition (PLD) [13-15], thermal evaporation [8, 16] and Chemical Vapour Deposition (CVD) [17].

Thermal oxidation technique is a relatively low-cost technique; it requires a furnace with a primary vacuum pump in order to reach the desired pressure. It guarantees high yield of production and does not require hazardous precursors. Moreover, the metallic layer, needed for the formation of the metal oxide nanowires, can be provided in thin film form directly on the final device for a direct integration, without the need of expensive and time consuming transfer procedures. Thus, the nanowires grow directly on the transducer enhancing the mechanical stability of the nanostructures essential for a potential commercialization of a real device.

In this work, WO_3 nanowires have been synthetized by thermally oxidizing a metallic tungsten film deposited by RF magnetron sputtering on alumina substrates for the preparation of chemical sensors for the first time to the best of our knowledge. The morphology and the structure of the nanowires were investigated, and chemical sensing performances were tested towards specific chemical species.

B Experimental

We used alumina substrates (2 mm x 2 mm, 99% purity) to synthetize tungsten oxide nanostructures.

For morphological investigation, four different batches have been prepared. We deposited a very thin metallic tungsten layer (18 nm) via RF magnetron sputtering (100 W argon plasma, $5.5x10^{-3}$ mbar) on two sets of samples, whereas on the others layer's thickness was increased to 180 nm. In case of one batch of 18nm samples and one of 180nm, sputtering temperature was set at 300°C, while in the others two batches was set at 200°C, in order to identify the influence of the temperature during film deposition.

Afterwards, samples were oxidized in a tubular furnace at 550°C for one hour, in order to promote the growth of the nanowires. Pressure inside the alumina tube was set at 0.8 mbar, with an oxygen flow of 2 SCCM.

A field-emission scanning electron microscope (FE-SEM) LEO 1525 was operated at 3-5kV, in order to investigate the morphology of the nanostructures. The microscope was coupled with an Energy Dispersive X-ray Analysis (EDX) INCA microanalysis system (Oxford Instruments, UK), to confirm the elemental composition and the stoichiometry of the material. EDX spectrum was recorded in the 0-10 keV range, recording the energy of X-Rays emitted by the samples impacted by a 10kV electron beam.

X-ray diffraction spectroscopy (XRD) was performed using an Empyrean diffractometer (PANalytical, Almelo, The Netherlands) mounting a Cu-LFF (λ = 1.5406 Å) tube operated at 40kV-40mA. XRD spectra were recorded by a parallel-plate collimated proportional Xe detector with a nickel large-β filter, in glancing-angle mode in the range of 5-90 degree (ω=1.0°). For XRD investigation, tungsten oxides nanowires were synthetized on 10x10 mm glass substrates.

Raman spectra were measured by HORIBA monochromator iHR320 configured with a grating of 1800 g/mm, coupled to a Peltier-cooled Synapse CCD. A He-Cd laser (442 nm) was focused on the samples by a fiber coupled confocal optical microscope (HORIBA) at 100x magnification. Spectra were recorded in the wavelength range 200-1200 cm^{-1}.

Two different set of samples were prepared for gas-sensing measurements (18nm and 180nm, 100 W argon plasma, 300°C, 5.5x10^{-3} mbar), to evaluate the influence of layer thickness in the response.
A two-steps deposition was used to fabricate the soldering pads for the sensing devices. Firstly we deposited a TiW adhesion layer by DC magnetron sputtering (70 W argon plasma, 300 °C, 5.5x10^{-3} mbar), to enhance mechanical properties during the soldering process. Then we deposited interdigited platinum contacts, using the same condition described before. Since metal oxide chemical sensing performances are strongly thermally activated, a platinum heater was deposited on the back-side of alumina substrates via the same two-steps technique used for contacts. The prepared devices were finally mounted on TO packages using electro-soldered gold wires. In order to stabilize the contact material, sensors were aged at 400 °C for 72 hours prior to the electrical measurements.

We used a flow-through technique to investigate the conductometric response of fabricated sensors, as reported in our previous works [18]. Devices were placed inside a home-made stainless-steel chamber (1 L of volume) located inside a climatic chamber (Angelantoni, Italy, model MTC 120), set at 20 °C to reduce the influence of external temperature variations. Temperature of sensors was controlled by modulating the electric power applied to heaters by Thurlbly-Thandar PL330DP power supplies.
Sensors were heated inside the chamber at desired working temperature for 8 hours for thermal stabilization, in presence of a humid air flow of 200 SCCM. Humidified air was produced by flowing synthetic dry air (SIAD SpA, Italy) through a Drechsel bottle, held in a thermostatic bath at 25 ◦C, and then in a condensation vessel in order to favour the condensation of saturated vapour. The humidified air was then mixed with synthetic dry air in order to obtain the desired relative humidity (RH) content. A humidity sensor (Vaisala, Finland, model HMI 36) was used to monitor the atmosphere of the test chamber and to adjust the flows of dry and humid air.
Test gases with a certified composition, supplied by SIAD SpA, (Italy) were mixed in a carrier of dry synthetic air by MKS Instrument mass flow controllers, maintaining the 200 SCCM total flow. Gas concentrations were chosen based on a possible target application. For example, the maximum concentration for ammonia was the human odour threshold (≈5 ppm). After the 30 min exposure to a fixed concentration of target gas, synthetic air flow was restored for 30 min, to allow the recovery of the baseline. A fixed voltage was applied to the sensors (Agilent E3631A power supply), typically 0.5–1 V, measuring at the same time the conductance of each sensor using dedicated picoammetters (Keithley 486). The response is determined by the variation of the conductance using the following formulas[19] for reducing and oxidizing gases, respectively:

$$Response = \frac{R_{Gas}-R_{Air}}{R_{Air}} = \frac{G_{Air}-G_{Gas}}{G_{Gas}} \quad (1)$$

$$Response = \frac{G_{Gas}-G_{Air}}{G_{Air}} \quad (2)$$

Where $\boldsymbol{R_{Gas}}$ and $\boldsymbol{G_{Gas}}$ are respectively the sensor resistance and conductance in presence of gas, and $\boldsymbol{R_{Air}}$ and $\boldsymbol{G_{Air}}$ in synthetic air.
As a preliminary investigation to determine the performance class of the material a temperature screening was performed, in order to determine optimal working temperature ranges for acetone, nitrogen dioxide, ethanol, carbon monoxide and ammonia. For a possible future commercialisation of the devices further investigastions will be necessary. Relative humidity was kept at 50% @ 20 °C during screening measurements.
Influence of humidity in the response was evaluated in presence of some gases, specifically nitrogen dioxide, carbon monoxide and ammonia, at the selected temperature of 200 °C.

C Results and Discussion

We investigated the influence of both metal layer thickness and sputtering temperature on the morphology of tungsten oxide nanowires. In Figure 1 are reported SEM pictures of samples of all four batches.

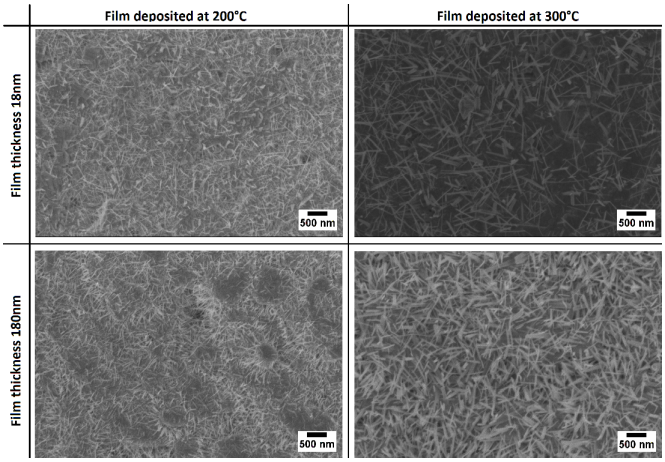

Figure 1: SEM pictures of oxidized 18nm and 180nm tungsten films deposited at different temperature by RF magnetron sputtering

The sputtering temperature of the tungsten film seems to have a strong influence on the size of the nanowires. Nanowires grown starting from a 300°C metal layer are bigger in both diameter and length compared to those grown from a 200°C, but in both cases the average diameter is less than 40 nm. Moreover, NWs synthetized from a layer deposited at 200°C exhibit less variability in diameter size, while for 300°C there is a larger spread of values. In Figure 2 is reported a statistical analysis on nanowire diameters for both temperatures.

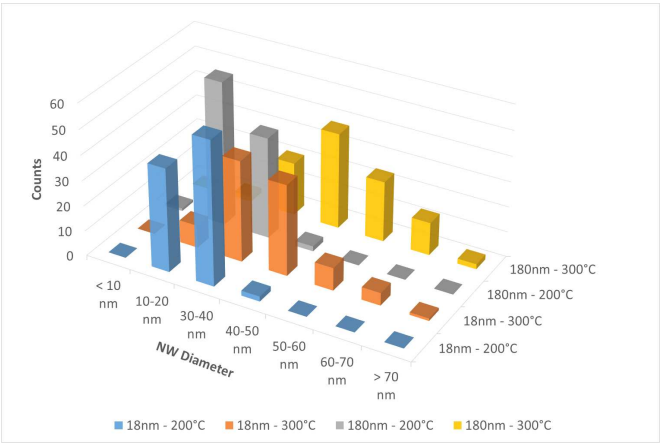

	18nm - 200°C	18nm - 300°C	180nm - 200°C	180nm - 300°C
μ (nm)	21,36	31,27	19,57	37,78
σ (nm)	4,20	9,44	4,56	10,32

Figure 2: Diameter distribution of WO_3 NWs grown on alumina substrate starting from different metallic W layers deposited at different temperatures.

Layer thickness has not much influence on diameter size at 200°C, but has a strong influence on the density of nanowires. This is probably due to the abundance of bulk tungsten material nanowires grow from. At 300°C instead, layer thickness has a slight influence on size also: an increase on the thickness results in an increase of the average diameter (≈31nm vs ≈38nm).

X-ray diffraction was performed in glancing-angle working mode on WO_3 nanostructures grown from 180nm metal film on glass substrate. Measured spectrum is reported in Figure 3 in the blue colour. Despite some peaks could be related to tungsten trioxide phase, reported in green colour in Figure 3, others may be related to metallic tungsten also (magenta-coloured peaks). This confirms the presence of a residual metallic tungsten layer beneath the nanostructures. Moreover, it has been reported in literature that the stoichiometry of tungsten oxide is very sensitive to deposition conditions [20]. In particular, if the WO_{3-y} material is strongly under-stoichiometric (y>0.5) it exhibits a yellow-metallic colour. On the contrary, stoichiometric WO_3 is transparent, or blue-coloured if slightly under-stoichiometric (y<0.5). Energy Dispersive X-ray Analysis (EDX) performed on as-prepared samples confirms that they are strongly under-stoichiometric, exhibiting a metallic yellow colour with an estimated y higher than 2.05.

However, it should be noted that prior to gas-sensing characterization samples undergone a thermal annealing for several hours at 400°C in air, in order to stabilize the baseline. We performed the same thermal treatment on the sample and we measured the XRD spectrum once again to verify the complete oxidation of the sample (Figure 3, red spectrum). Finally, there is no sign of residual metallic tungsten, meaning that samples for gas-sensing measurements were crystalline and stoichiometric, becoming transparent also. EDX investigation confirms the typical stoichiometry of bulk WO_3, with a y lower than 0.15.

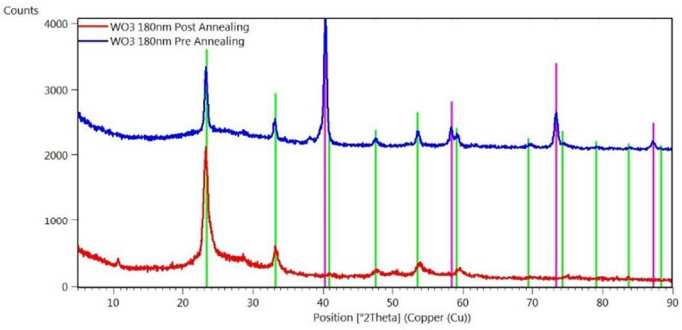

Figure 3: X-Ray Diffraction (XRD) spectra of WO_3 180nm before (blue) and after annealing (red), and reference peaks of metallic W (magenta) and WO_3 (green). Spectra shifted in intensity for clarity purpose.

Tungsten oxide nanowires and films are composed of a network of corner-shared WO_6 octahedron units [14]. These units are supposed to be connected to each other by W–O–W or hydrogen bonds through water bridges, with terminal W=O bonds at the surface of the clusters [21].
Figure 4 reports the Raman spectrum of tungsten oxide nanostructures synthetized from a 180nm tungsten film in comparison with the alumina spectrum from the substrate. The shape of the two spectra is quite different. There is no sign of Al_2O_3 peaks in the WO_3 spectrum; therefore, the film covers uniformly the substrate.

The vibration frequency of W=O double bound is expected to be higher than that of W-O bond, due to the stronger bonding energy, and is usually located about at ≈950 cm^{-1}. This peak generates from stretching modes (v_s) of the surface terminal W=O caused by absorbed water molecules, and is frequently seen in sputtered or evaporated films deposited at lower temperatures [20, 22]. The very low intensity of the measured peak in our samples means that comparably small amounts of water were absorbed in our nanowires. Moreover, according to the literature [23] the position of the W=O bond (range 930-975 cm^{-1}) depends also on the tungsten content: the higher the tungsten content, the higher the Raman frequency appears.

The peaks sited at 798 cm^{-1} and 705 cm^{-1} are typical Raman peaks of monoclinic crystalline WO3, which corresponds to W-O-W stretching vibrations of the bridging oxygen [14, 24]. The additional peaks at 264 and 321 cm^{-1} are due to the bending vibration δ(O-W-O) [14].

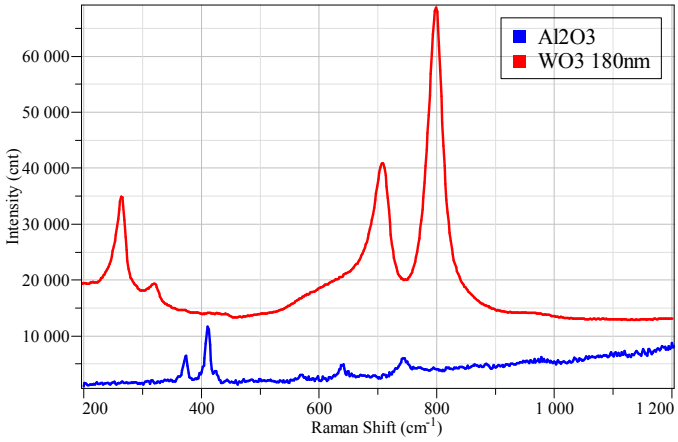

Figure 4: Raman spectra of WO_3 180nm and alumina substrate. Spectra shifted in intensity for clarity purpose.

After the morphological and structural characterization, gas-sensing measurements have been performed. A temperature screening have been performed on both 18nm and 180nm devices, in order to determine the optimal working temperature for each target gas. Temperature was modulated from 100°C to 400°C, and the sensors were exposed to fixed concentrations of CH_3CH_2OH, CO, NO_2, NH_3 and CH_3COCH_3. In Figure 5 we report an example of the dynamic measurement obtained by both 18 and 180 nm devices. In presence of an oxidizing chemical species, like NO_2, we observe a decrease in the electrical conductance, while we measure an increase of the conductance in presence of reducing gases like ethanol and carbon monoxide. This behavior is typical of n-type semiconductors, like tungsten oxide.

According to literature [25, 26], when n-type tungsten oxide is exposed to air we have the adsorption of oxygen molecules on the surface of the nanostructures. These adsorbed molecules interact with the oxide surface, subtracting electrons from the nanowires and forming adsorbed O_2^-, O^- and O^{2-} ions, lowering the electrical conductance of the material. In presence of oxidizing gases, like NO_2 for example, the interaction of gas molecules with oxide surface leads to an increase of the number of adsorbed ions, reducing the density of free electrons and thus decreasing the electrical conductance of the devices. In particular, for NO_2 the following reactions could explain this decrease in the conductance of sensors [25]:

$$NO_2\,(g) + e^- \leftrightarrow NO_2^-\,(ads) \quad (3)$$

$$NO_2\,(g) + e^- \leftrightarrow NO(g) + O^-\,(ads) \quad (4)$$

On the other hand, when a reducing gas is introduced in the measuring chamber, adsorbed gas molecules interact with adsorbed oxygen ions, releasing charge carriers (electrons for n-type semiconductors) and thus increasing the electrical conductance. This behaviour could be explained for i.e. ammonia according to the following equations [26]:

$$2NH_3\,(ads) + 3/2O_2^-\,(ads) \leftrightarrow N_2 + 3H_2O + 3e^- \quad (5)$$

$$2NH_3\,(ads) + 3O^-\,(ads) \leftrightarrow N_2 + 3H_2O + 3e^- \quad (6)$$

$$2NH_3\,(ads) + 3O^{2-}\,(ads) \leftrightarrow N_2 + 3H_2O + 6e^- \quad (7)$$

It worth to note that in [26] the change in the electrical resistance was attributed to two different mechanisms. The first one was a decrease in the surface resistivity of WO_3 nanowires due to the increased free electron density, while the second one was a decrease in the barrier height at the boundary between nanocrystallines along the nanowire. Unlike the previous work, thermally oxidized nanowires are highly crystalline, and thus the second mechanism is probably involved only in the junctions between different nanowires on the substrate, suggesting that the first sensing mechanism is likely dominant.

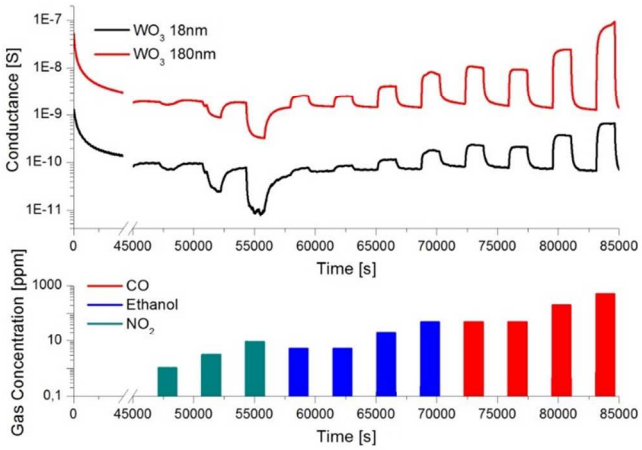

Figure 5: Dynamic response of WO_3 sensing devices towards some oxidizing (NO_2, aquamarine colour, 1-3-9 ppm) and reducing (Ethanol, blue colour, 5-5-20-50 ppm) (Carbon Monoxide, red colour, 50-50-200-500 ppm) gas chemical compound, measured at 200°C with a relative humidity of 50% @ 20°C.

We report the sensing response of fabricated devices in Figure 6. The temperature dependence of 180nm and 18nm devices is

almost the same. However, the overall sensing performances of 180nm devices almost always overtake the 18nm ones. This could be due to the different density of nanostructures on the substrate. Device fabricated starting from a 180nm metal film exhibit a higher density of nanowires compared to 18nm ones. The increased surface area could reflect in better sensing performances.

At relatively low temperatures (<300°C) devices are more sensitive to CO, NO_2 and NH_3. In particular, 200°C results the optimal temperature for the detection of carbon monoxide and ammonia. For ethanol, the optimal working temperature is 300°C, even if the temperature influence on the response is less evident than CO and NH_3. The response of 180nm devices in presence of 100ppm of acetone increase as we increase the working temperature, reaching its maximum at 400°C. It is interesting to note that, at low temperatures, devices are more sensitive to ethanol, while at high temperatures sensors detect acetone more easily. It is thus possible to tune the working temperature of devices in order to increase the selectivity between these two volatile organic compounds, depending on the requested application. For NO_2 we obtain a slightly higher optimal working temperature compared to other metal oxide materials, like SnO_2 [27].

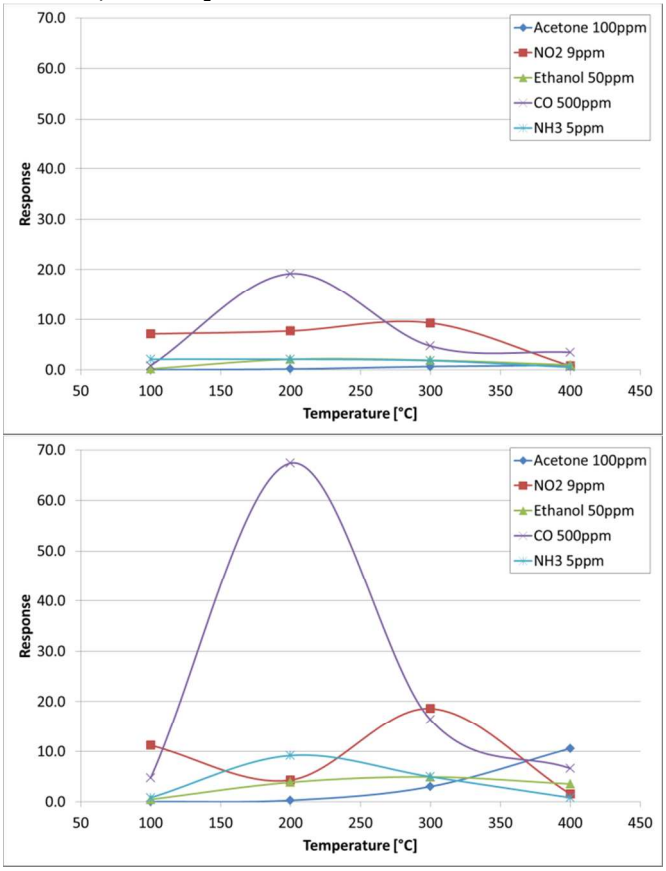

Figure 6: Temperature dependence of the response of 18nm (left) and 180nm (right) WO_3 nanostructures, measured with a relative humidity of 50% @ 20°C. Target chemical species used: Acetone 100ppm (blue), Nitrogen Dioxide 9ppm (red), Ethanol 50ppm (green), Carbon Monoxide 500ppm (purple), Ammonia 5ppm (cyan).

Preliminary calibration curves have been estimated, inletting in the chamber fixed concentration of some target gases, like CO, NO_2 and NH_3, and measuring the conductance variations at the optimal working temperature (RH=50%@20°C) for each gas. For CO and NH_3 we choose the most sensitive temperature of 200°C, while for NO_2 we choose 100°C. Even if this is not the optimal working temperature for NO_2, this is a good tradeoff between performances and power consumption, from an energy saving point-of-view. The experimental data could be fitted by the typical power trend relation for metal oxide sensors:

$$Response = A[gas\ concentration]^B \quad (8)$$

where A and B are constants typical of the sensing material and the stoichiometry of the involved reactions. Table 1 reports A and B coefficient values and estimated detection limits for three target gases (CO, NO_2 and NH_3), considering a response of 1 as the minimum response in order to have an appreciable signal. The slope of trends line for NO_2 and CO is quite similar, even if the working temperature of sensors is not (Figure 7). For NH_3 instead, the slope of the estimated calibration curve is higher than the other two curves, and devices perform exceptionally well. It's interesting to note that the ratio between the response towards 5ppm of NH_3 and the same concentration of other target gases is often more than one order of magnitude, indicating a good selectivity towards ammonia (≈100 for acetone, ≈2.5 for NO_2, ≈10 for CO and ≈15 for ethanol, at 200 °C and RH=50%@20°C).

	Working Temperature	Detection Limit	B	A
CO	200 °C	13 ppm	1.15	0.05
NO2	100 °C	1 ppm	1.23	0.87
NH3	200 °C	1.5 ppm	2.04	0.5

Table 1: Power trend line coefficients and detection limits towards CO, NO_2 and NH_3.

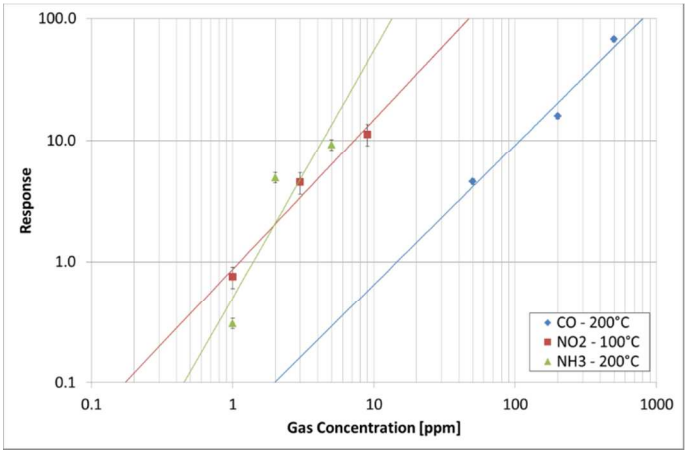

Figure 7: Detection trend lines for 180nm devices towards CO (200°C, blue), NO_2 (100°C, red) and NH_3 (200°C, green). Relative humidity was 50% @ 20°C

The sensing performances of fabricated nanostructures have been compared to other devices reported in literature. Considering CO as a target gas, sensors integrating 180 nm WO_3 nanostructures outmatch the performance of both 18 nm and other pure [28], Fe-doped [4] and photo-activated [29] WO_3 thin films, even if in some cases we must take into account a slightly different working temperature (Figure 8). Fabricated devices largely outperform [26] in NH_3 detection, probably due to higher crystallinity of the nanostructures.

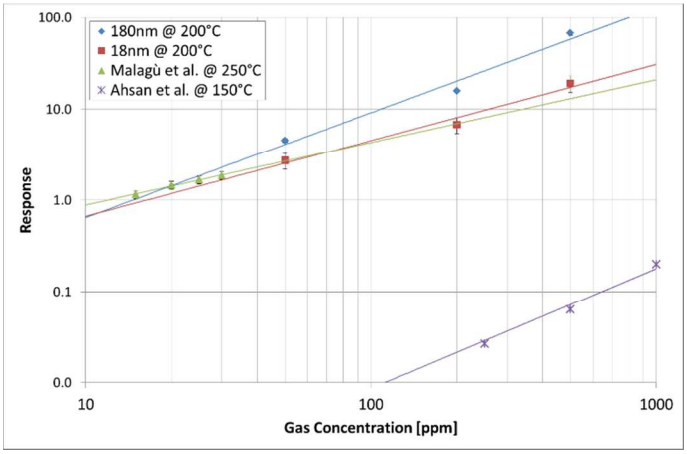

Figure 8: Carbon monoxide (CO) sensing performance comparison between fabricated WO_3 nanostructures (18 nm and 180 nm) and reference literature, in particular *Ahsan et al.* [4] and *Malagù et al.* [29].

Influence of the humidity was taken into account also. Figure 9 reports the response of samples prepared from 180 nm film towards NO_2, CO and NH_3, at different humidity ratios. These values have been normalized respect a relative humidity of 50% @ 20°C, while the operating temperature was kept at 200°C in all measurements. The response of the devices towards nitrogen dioxide and ammonia was greatly reduced in presence of dry air, which probably means that water molecules adsorbed on the oxide surface play some role in the sensing mechanism. On the opposite, carbon monoxide sensing seems to prefer a dry airflow. In standard environmental conditions (RH of 25%-50%) the effect of humidity on sensors response is between 80% for CO and NH_3, and 150% of NO_2. It is interesting to note that influence of humidity on NH3 detection is almost negligible in a range of RH of 25%-75%, while NO_2 detection is very sensitive to humidity instead.

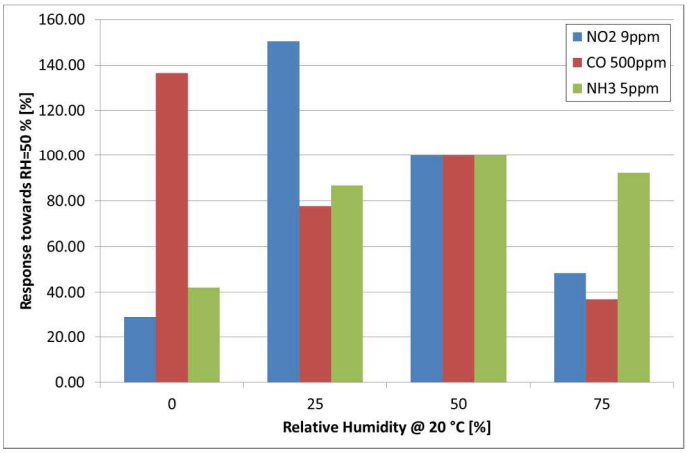

Figure 9: Influence of humidity on WO_3 180nm device response towards nitrogen dioxide, carbon monoxide and ammonia. On the y-axis the ratio between the response at the target value of relative humidity respect the reference value of RH=50% @ 20°C. Sensors temperature fixed @ 200°C.

Conclusions

Conductometric tungsten oxide gas-sensing devices were successfully fabricated on 2x2mm alumina substrates. The morphology of the nanostructures was characterized by mean of scanning electron microscopy, resulting in a mat of nanowire-like structures. X-ray diffraction and Raman spectroscopies confirmed the phase and crystallinity of the material. Fabricated conductometric sensing devices were mounted inside a custom test chamber, in order to measure conductance variations in presence of some target chemical species (CH_3CH_2OH, CO, NO_2, NH_3 and CH_3COCH_3). Sensing performances were very interesting. Devices fabricated starting from a 180nm tungsten film always outperform ones fabricated from a 18nm film, and they perform better than similar devices reported in literature also, especially for ammonia detection. Moreover, devices exhibit a good selectivity toward this chemical species compared to same concentration of other target gases. The influence of the humidity on the response was evaluated also, resulting in a stable response towards ammonia in the 25%-75% RH range. Future activities should be carried out to exactly determine the optimal working temperature of devices with respect to the target chemical compound, and to establish full-range calibration curves. However, these preliminary investigations make tungsten oxide nanowires an ideal candidate for the fabrication of ammonia gas sensing devices.

Acknowledgements

The work has been supported by the Italian MIUR through the FIRB Project RBAP115AYN "Oxides at the nanoscale: multifunctionality and applications". This work was partially supported by the European Community's 7th Framework Programme, under the grant agreement n° 246334 "Orama: Materials for the Post-Silicon Electronics Era" and under the grant agreement n° 611887 "MSP: Multi Sensor Platform for Smart Building Management".

Notes and references

1. M. Furubayashi, K. Nagato, H. Moritani, T. Hamaguchi and M. Nakao, *Microelectron Eng*, 2010, 87, 1594-1596.
2. Y. Kojima, K. Kasuya, T. Ooi, K. Nagato, K. Takayama and M. Nakao, *Japanese Journal of Applied Physics Part 1-Regular Papers Brief Communications & Review Papers*, 2007, 46, 6250-6253.
3. S. H. Baeck, K. S. Choi, T. F. Jaramillo, G. D. Stucky and E. W. McFarland, *Adv. Mater.*, 2003, 15, 1269-+.
4. M. Ahsan, T. Tesfamichael, M. Ionescu, J. Bell and N. Motta, *Sens. Actuator B-Chem.*, 2012, 162, 14-21.
5. T. Maekawa, J. Tamaki, N. Miura and N. Yamazoe, *Chem Lett*, 1992, DOI: Doi 10.1246/Cl.1992.639, 639-642.
6. M. H. Yaacob, M. Breedon, K. Kalantar-Zadeh and W. Wlodarski, *Sens. Actuator B-Chem.*, 2009, 137, 115-120.
7. S. An, S. Park, H. Ko and C. Lee, *Ceram Int*, 2014, 40, 1423-1429.
8. N. V. Hieu, H. V. Vuong, N. V. Duy and N. D. Hoa, *Sens. Actuator B-Chem.*, 2012, 171, 760-768.
9. E. Salje, *Acta Crystallogr A*, 1975, A 31, 360-363.
10. L. E. Depero, S. Groppelli, I. NataliSora, L. Sangaletti, G. Sberveglieri and E. Tondello, *Journal of Solid State Chemistry*, 1996, 121, 379-387.
11. E. Lassner and W. D. Schubert, *Tungsten: Properties, Chemistry, Technology of the Elements, Alloys, and Chemical Compounds*, Springer US, 1999.
12. M. Szabo, P. Pusztai, A. R. Leino, K. Kordas, Z. Konya and A. Kukovecz, *J Mol Struct*, 2013, 1044, 99-103.
13. K. J. Lethy, D. Beena, R. V. Kumar, V. P. M. Pillai, V. Ganesan and V. Sathe, *Appl Surf Sci*, 2008, 254, 2369-2376.
14. A. Rougier, F. Portemer, A. Quede and M. El Marssi, *Appl Surf Sci*, 1999, 153, 1-9.
15. S. Yamamoto, A. Inouye and M. Yoshikawa, *Nucl. Instrum. Methods Phys. Res. Sect. B-Beam Interact. Mater. Atoms*, 2008, 266, 802-806.
16. S. Y. Ma, M. Hu, P. Zeng, M. D. Li, W. J. Yan and C. Q. Li, *Materials Letters*, 2013, 112, 12-15.
17. R. Huang, J. Zhu and R. Yu, *Chinese Phys B*, 2009, 18, 3024-3030.
18. G. Sberveglieri, G. Faglia, C. Perego, P. Nelli, R. N. Marks, T. Virgilli, C. Taliani and R. Zambonin, *Synth. Met.*, 1996, 77, 273-275.
19. *Solid State Gas Sensing*, Springer, New York, 2009.
20. J. G. Zhang, D. K. Benson, C. E. Tracy, S. K. Deb, A. W. Czanderna and C. Bechinger, *J Electrochem Soc*, 1997, 144, 2022-2026.
21. Y. Shigesato, Y. Hayashi, A. Masui and T. Haranou, *Jpn J Appl Phys 1*, 1991, 30, 814-819.
22. M. F. Daniel, B. Desbat, J. C. Lassegues, B. Gerand and M. Figlarz, *Journal of Solid State Chemistry*, 1987, 67, 235-247.
23. D. Gazzoli, M. Valigi, R. Dragone, A. Marucci and G. Mattei, *Journal of Physical Chemistry B*, 1997, 101, 11129-11135.
24. B. M. Weckhuysen, J. M. Jehng and I. E. Wachs, *Journal of Physical Chemistry B*, 2000, 104, 7382-7387.
25. H. J. Xia, Y. Wang, F. H. Kong, S. R. Wang, B. L. Zhu, X. Z. Guo, J. Zhang, Y. M. Wang and S. H. Wu, *Sens. Actuator B-Chem.*, 2008, 134, 133-139.
26. V. H. Nguyen, V. Q. Vu, D. H. Nguyen and D. Kim, *Curr Appl Phys*, 2011, 11, 657-661.
27. N. M. Shaalan, T. Yamazaki and T. Kikuta, *Sensors and Actuators B: Chemical*, 2012, 166–167, 671-677.
28. A. Ponzoni, E. Comini, M. Ferroni and G. Sberveglieri, *Thin Solid Films*, 2005, 490, 81-85.
29. C. Malagu, M. C. Carotta, E. Comini, G. Faglia, A. Giberti, V. Guidi, T. G. G. Maffeis, G. Martinelli, G. Sberveglieri and S. P. Wilks, *Sensors-Basel*, 2005, 5, 594-603.